ACS APPLIED MATERIALS & INTERFACES

Research Article

www.acsami.org

Au Nanoparticles–3D Graphene Hydrogel Nanocomposite To Boost Synergistically in Situ Detection Sensitivity toward Cell-Released Nitric Oxide

Jialin Li,[†,‡,§] Jiale Xie,[†,‡,§] Lixia Gao,[†,‡,§] and Chang Ming Li*[,†,‡,§]

[†]Institute for Clean Energy & Advanced Materials and [‡]Faculty of Materials and Energy, Southwest University, Chongqing 400715, China

[§]Chongqing Key Laboratory for Advanced Materials and Technologies of Clean Energies, Chongqing 400715, China

ABSTRACT: In situ detection of nitric oxide (NO) released from living cells has become very important in studies of some critical physiological and pathological processes, but it is still very challenging due to the low concentration and fast decay of NO. A nanocomposite of Au nanoparticles deposited on three-dimensional graphene hydrogel (Au NPs–3DGH) was prepared through a facile one-step approach by in situ reduction of Au^{3+} on 3DGH to build a unique sensing film for a strong synergistic effect, in which the highly porous 3DGH offers a large surface area while Au NPs uniformly deposited on 3DGH efficiently catalyze the electrochemical oxidation of NO for sensitive detection of NO with excellent selectivity, fast response, and low detection limit. The sensor was further used to in situ detect NO released from living cells under drug stimulation, showing significant difference between normal and tumor cells under drug stimulation.

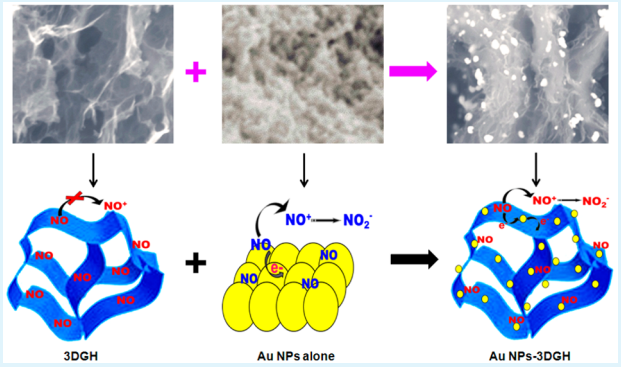

KEYWORDS: *Au nanoparticles, graphene hydrogel, nitric oxide, in situ detection, JB6-C30, B16-F10*

1. INTRODUCTION

Nitric oxide (NO) plays various important roles in biological systems. Besides its physiological characters in neurotransmission,[1−3] immune defense function,[4,5] and vasorelaxation,[6] NO is also critical in pathology related to carcinogenesis promotion and conductive or detrimental tumor progression,[7,8] as well as the pathogenesis of some diseases.[9] In situ detection of NO is important to understand the mechanisms of some fatal diseases, such as atherosclerosis occurring in blood vessels,[10−12] and has been extensively developed in recent years to investigate physiological and pathological progress involving NO, while also being used for clinic diagnosis, thus rendering it of great significance in both science and medical applications.[13] However, nitric oxide is a very chemically active species that can be quickly oxidized by oxygen or superoxide NO_2^- or NO_3^- ions. It has a short half-life of 6 s in physiological solutions.[14,15] Therefore, it is difficult to sensitively detect nitric oxide, even with an in situ detection approach for living cells, which have very low concentrations and too many interference species.

Different methods, including chemiluminiscence,[16,17] fluorometry,[18,19] electron spin resonance (ESR),[20,21] and electrochemistry,[22,23] have been developed to in situ detect nitric oxide in tissues or cell cultures. However, chemiluminescence requires additional reagents to react with NO as a luminous source[24] and a fluorescent[25] or a spin-trapping NO compound[26] for generating detectable signals and has poor selectivity.[27] Fluorometric assays are not reproducible, and some probes are pH-sensitive, affecting the sensitivity of the method.[28,29] ESR needs special handling and specific experimental conditions, such as low temperature operation and long recording time.[26,30] In contrast, the electrochemical method is simple, sensitive, portable, selective, fast, and miniaturizable;[31,32] thus, it is an advantageous method to achieve real-time and in situ monitoring of nitric oxide in biological samples.[29,31,33]

To in situ detect NO in living cells, a miniaturized probe is critical to allow penetration into a single cell. Various microelectrodes, such as carbon fiber[34,35] or a platinum[36] or gold microelectrode,[37] have been developed to detect nitric oxide, since the first electrochemical detection of NO was based on a Clark-type platinum electrode.[38] Nevertheless, microelectrodes still suffer from strong interferences, low signal-to-noise ratio (S/N ratio), and poor reusability.[32,39] The miniaturization of a microelectrode also trades out its detection sensitivity.[29] Recently, with the advances of nanoscience, electrochemical sensors with superior nanostructure, high surface area, good conductivity, biocompatibility, high catalytic

Received: November 7, 2014
Accepted: January 12, 2015
Published: January 12, 2015

DOI: 10.1021/am5077777
ACS Appl. Mater. Interfaces 2015, 7, 2726−2734

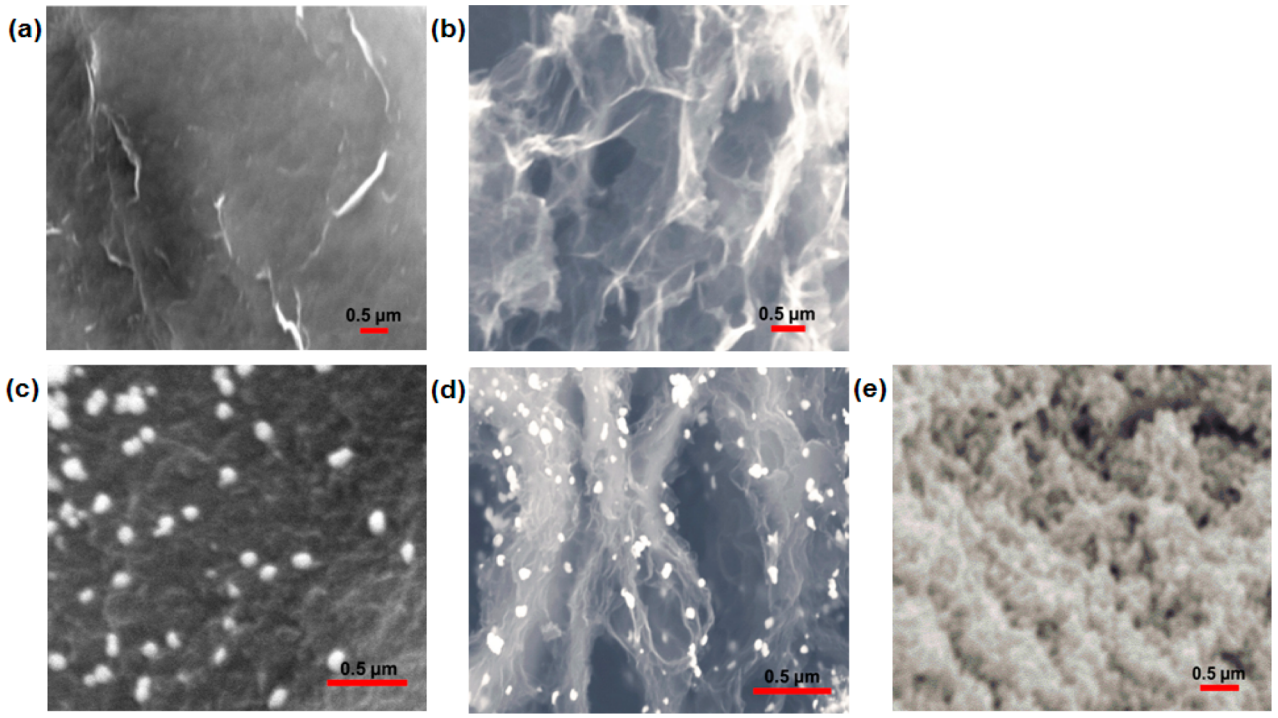

Figure 1. SEM images: (a) graphene, (b) 3DGH, (c) Au NPs−G, (d) Au NPs−3DGH, and (e) Au NPs alone.

activity, and unique chemical modifications have been used to in real time and in situ detection of NO,[32,40,41] but highly sensitive and selective electrochemical sensors are still highly desired.

Graphene (G), structured by a single layer of carbon atoms patterned in a hexagonal lattice, has attracted much attention.[42] Three-dimensional graphene hydrogel (3DGH) can be expected to further improve the physical and electrochemical properties of graphene for various important electrochemical applications due to its flexible, porous, and 3D-networked structure,[43] which enjoys excellent conductivity, high specific surface area, and fast charge mobility.[44] Moreover, the central hollow cores and the outside walls of 3DGH could efficiently adsorb and store gases. Nevertheless, 3DGH has poor intrinsic electrocatalytic activity due to its carbon nature. Since gold nanoparticles (Au NPs) have been recognized as an efficient electrocatalyst toward the oxidation of NO, for the first time, a facile one-step in situ reduction approach is developed in this work to produce a functional Au NPs−3DGH nanocomposite for synergistic enhancement of the electrocatalytic performance toward NO oxidation. The as-prepared material was further used as a NO sensor to detect highly sensitively and selectively in situ NO released from living tumor cells. The difference between NO released from the normal and tumor cells was studied to provide fundamental insights toward the understanding of the progress of melanoma.

2. EXPERIMENTAL SECTION

2.1. Preparation of Au NPs−3DGH Composite and Its Modified Electrode. 3DGH was prepared first by a one-step self-assembling process, in which an aqueous dispersion of homogeneous graphene oxide (GO) (2.5 mg/mL) was sealed in a Teflon-lined autoclave and heated at 180 for 12 h.[43] Then the 3DGH was obtained by freeze-drying the product while its high flexible structure was maintained. Graphene (G) was synthesize by adding vitamin C (2 mM) in a 0.1 mg/mL GO solution of pH 10.5, followed by heating to 90 °C with stirring until the GO solution turns brown or black. Then the product G was centrifuged and dried.

Then Au NPs−3DGH was prepared through a simple one-step in situ reduction of Au^{3+} constructed on the 3DGH, in which 3DGH acted as an excellent conducted matrix, while Au NPs were directly grown on the 3D surface of the graphene hydrogel. The freeze-dried 3DGH was added to chloroauric acid solution (1 mM) with stirring for 15 min followed by adding 0.01 M ice-cooled $NaBH_4$ with stirring until the light-yellow solution turned to wine red, upon which it was filtrated to obtain the Au NPs−3DGH composite. For comparison, grapheme is used instead of 3DGH to prepare Au NPs−G with the same procedure.

Au NPs−3DGH was dissolved in Nafion solution (0.05%) for preparation of a 5 mg/mL solution, and the as-prepared solution (3.5 μL) was dropped and dried on a glassy carbon electrode (GCE) surface by surface immobilization.

2.2. Materials Characterizations. The morphologies of the as-prepared materials were investigated by scanning electron microscopy (SEM; JSM-6510LV). Their crystal structures were studied by transmission electron microscope (TEM; JEM-2100) and X-ray diffraction (XRD; XRD-7000).

All electrochemical measurements were carried out with a CHI 660C electrochemical analyzer (Shanghai Chenhua Co.) in a three-electrode system having a silver/silver chloride (Ag/AgCl), platinum filament, and GCE as reference, counter, and working electrode, respectively.

2.3. Preparation of Saturated NO in PBS. The saturated NO in PBS solution was prepared according to the reported procedure.[9] NO gas was generated by slowly dropping H_2SO_4 (2 M) into a glass flask containing saturated $NaNO_2$ solution after the devices was set up and degassed meticulously with nitrogen gas for 30 min to remove O_2. Then NO gases were sequentially passed through saturated potassium hydroxide solution and 10% (w/v) and 2.5% (w/v) potassium hydroxide solution to remove oxygen and other nitrogen oxides. The NO saturated concentration in solution was about 1.8 mM at 20 °C.

2.4. Cell Culture. The mice normal skin cells JB6-C30 and tumor cells B16-F10 were obtained from Chongqing University and Chongqing Medical University, respectively. The B16-F10 cells were maintained in complete Rosewell Park Memorial Institute medium (RPMI-1640) supplemented with 10% fetal bovine serum (FBS) and

DOI: 10.1021/am5077777
ACS Appl. Mater. Interfaces 2015, 7, 2726−2734

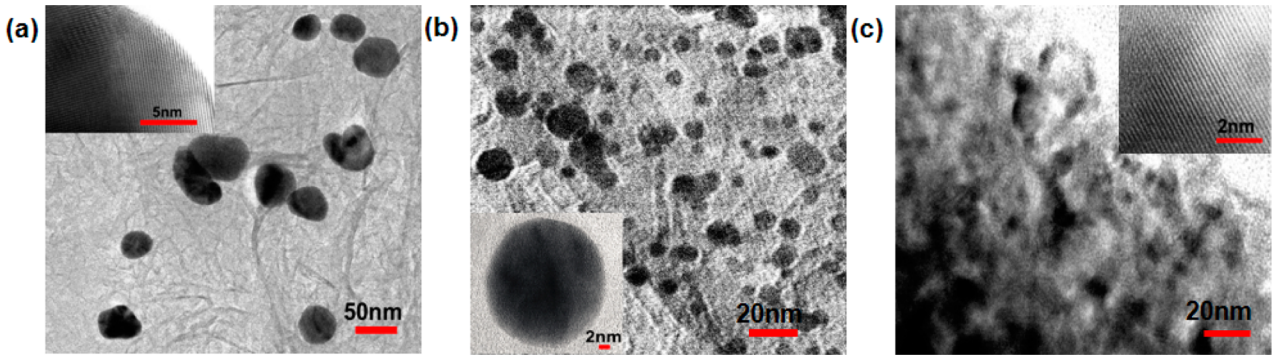

Figure 2. TEM images: (a) Au NPs−G, (b) Au NPs−3DGH, and (c) Au NPs alone.

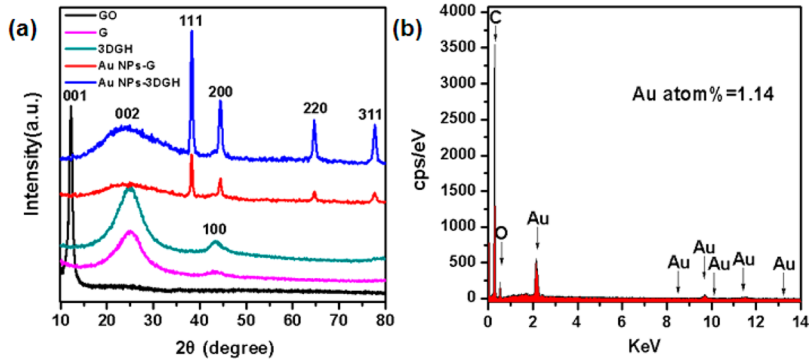

Figure 3. (a) XRD patterns of GO, graphene, 3DGH, Au NPs−G, and Au NPs−3DGH. (b) EDS image of 3DGH−Au nanocomposite.

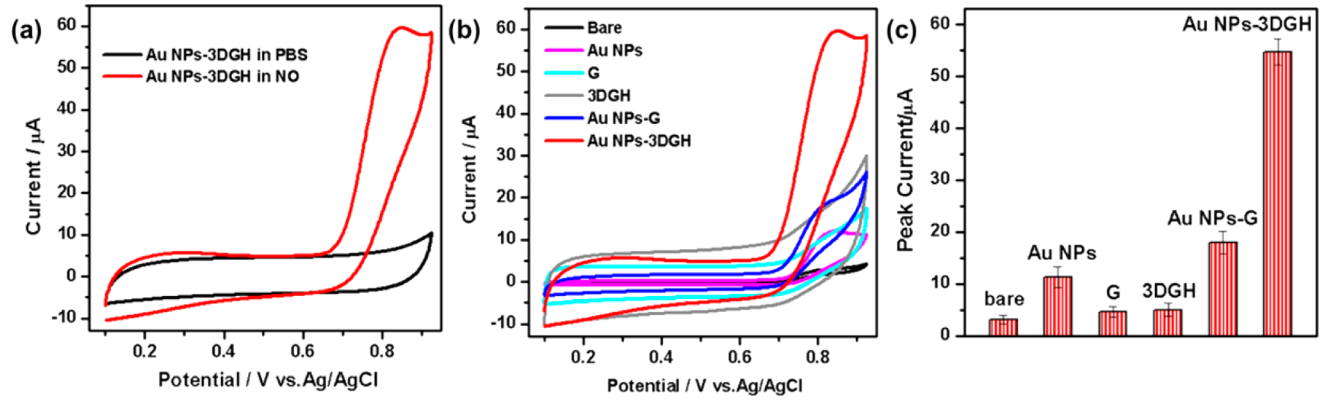

Figure 4. CV curves of different electrodes in 0.01 M PBS (pH 7.4) solution, at a scan rate of 50 mV/s: (a) Au NPs−3DGH modified electrode in the absence (black) and presence (red) of 0.5 mM nitric oxide. (b) Different modified electrodes in the presence of 0.5 mM nitric oxide: bare (black), Au NPs (magenta), G (light blue), 3DGH (gray), Au NPs-Graphene (blue), Au NPs−3DGH (red). (c) Response of the five different modified electrodes corresponding to part b.

1% mycillin, while JB6-C30 cells were cultured in Dulbecco's modified Eagle medium (DMEM) containing 10% FBS and 1% mycillin, and both were kept in a water-jacketed CO_2 incubator (Forma Series II) at 37.8 °C.

3. RESULTS AND DISCUSSION

The SEM images of the as-prepared materials G (a), 3DGH (b), Au NPs−G (c), Au NPs−3DGH composite (d), and Au NPs alone (e) are shown in Figure 1 for comparison, and they clearly revealing that the 3D graphene hydrogel has a three-dimensional (3D) porous networked structure and is flexible and fluffy. Au NPs can only deposit on the outer surface of graphene when they have large particle sizes, while Au NPs alone are conjugated together to form large aggregates. In contrast, the Au NPs−3DGH composite is much more porous with uniformly distributed, much smaller Au NPs in both the inner and outer networked surface in a diameter range over 5−40 nm. This should be mainly attributed to the porous, fluffy, networked structure of 3DGH and its highly concentrated surface active sites, which strongly absorb Au(III) complex to grow small Au NPs via reduction by $NaBH_4$.

The transmission electron microscopy (TEM) images of Au NPs−G (a), Au NPs−3DGH composite (b), and Au NPs alone (c) in Figure 2 show that the lattice spacing of Au NPs of all the materials is near 2.3 Å, which is in good agreement with that (2.34 Å) of the (111) plane of Au NPs, corresponding to the peak at 38° in the XRD pattern (Figure 3a). However, Au NPs−3DGH composite (b) has a more uniform distribution of small Au NPs (5−40 nm diameter) with retention of the

DOI: 10.1021/am5077777
ACS Appl. Mater. Interfaces 2015, 7, 2726−2734

porous structure of 3DGH after Au NPs incorporation, while Au NPs−G (a) has much fewer and nonuniformly distributed Au nanoparticles (15−50 nm). Au NPs (c) alone just completely coagulated together. The TEM results are in good agreement with the SEM ones.

Figure 3a shows X-ray diffraction (XRD) patterns of GO, G, 3DGH, Au NPs−G, and Au NPs−3DGH nanocomposite. The reflection peak (001) of GO at around 2θ = 10.8° has disappeared and new peaks at around 2θ = 25.9° and 43.5° corresponding to graphene are observed in both the G and 3DGH samples, confirming that both of them were effectively reduced. The peaks around 2θ = 38°, 44°, 65°, and 78° can be assigned to (111), (200), (220), and (311) planes of cubic-structured Au, respectively. It confirms that Au NPs−3DGH and Au NPs−G have the same composition and lattice structure, but with a stronger peak intensity for the former. The EDS image of 3DGH−Au nanocomposite (b) also shows that the composite is composed of carbon and Au.

To compare the electrocatalytic behaviors of different as-prepared electrodes, including bare/GCE, Au NPs/GCE, G/GCE, 3DGH/GCE, Au NPs−G/GCE, and Au NPs−3DGH/GCE, toward NO oxidation, cyclic voltammetry (CV) was performed, as shown in Figure 4, which demonstrate that for NO electrooxidation the plain G and 3DGH do not have significant oxidation current, while Au NPs, Au NPs−G, and Au NPs−3DGH electrodes exhibit high peak current in the order of Au NPs < Au NPs−G < Au NPs−3DGH; obviously, the Au NPs−3DGH nanocomposite electrode has the highest peak current.

The half-potential of an electrochemical reaction wave is often used to measure the electrode catalytic activity. The half-potentials of the electrooxidation peaks for various electrodes determined from Figure 4b are listed in Table 1, indicating an order of bare electrode (GC) = Au NPs > Au NPs−G > Au NPs−3DGH (the oxidation peaks for G and 3DGH are not well defined enough for calculation, showing their poor electroactivity toward NO oxidation). For an electrooxidation reaction, a more negative half-potential indicates that an oxidation peak possesses higher electrocatalytic activity. Apparently, Au NPs have almost the same intrinsic catalytic activity as GC, but their much higher peak current may indicate that Au NPs have more active reaction surface area than GC. Au NPs−G not only further enhances the electrocatalytic activity evidenced by its more negative half-peak potential but also shows higher peak current than both GC and Au NPs. More interestingly, Au NPs−3DGH results in dramatically increased anodic peak current and negatively shifted peak potential (red); the peak current is about 3 times larger than that of Au NPs−G and 4.5 times that of Au NPs alone, as shown in Figure 4c. This clearly indicates that Au NPs−3DGH nanocomposite offers a strong synergistic effect on the electrocatalysis toward NO oxidation rather than a simple sum of advantages from both composites.

Table 1. Catalytic Performance of Electrodes Modified with Different Materials toward 0.5 mM NO in 0.01 M PBS (pH 7.4) Solution

electrode	half-wave potential (V)	peak current (μA)
bare	0.772	3.065
Au NPs	0.774	11.345
G	0.781	4.594
3DGH	0.779	5.134
Au NPs−G	0.764	17.985
Au NPs−3DGH	0.750	54.642

The effect of Au^{3+} ($HAuCl_4$) concentration on the sensing performance of the as-prepared Au NPs−3DGH composite electrode was studied by CV in a concentration range of Au^{3+} over 0−10 mM. The plot of peak current versus concentration of Au^{3+} in Figure 5a shows that a Au^{3+} concentration of 1.2 mM is the optimal one to produce the best Au NPs−3DGH composite for the highest peak current. The effect of pH on Au NPs−3DGH modified electrode was also investigated to optimize the composite electrode performance for NO oxidation in 0.1 M PBS solutions containing 0.5 mM NO in a pH range of 6.5−8.5, as shown Figure 5b. It is found out that peak current increases with increasing pH, achieves the maximum at pH 7.0, and then decreases. Since pH 7.4 was close to the biological environment, all further electrochemical measurements were performed in PBS solution with pH 7.4.

In order to further understand the catalytic mechanism of the as-prepared material toward NO oxidation, CV for different modified electrodes was carried out at different scan rates from 2 to 150 mV/s in 0.01 M PBS (pH 7.4). Figure 6 shows that the relation of the anodic peak current to the square root of scan rate for both Au NPs−2DG and Au NPs−3DGH modified electrodes is linear, indicating a diffusion-controlled process toward NO electrooxidation. It is known that during NO electrochemical oxidation, NO loses an electron to form NO^+,

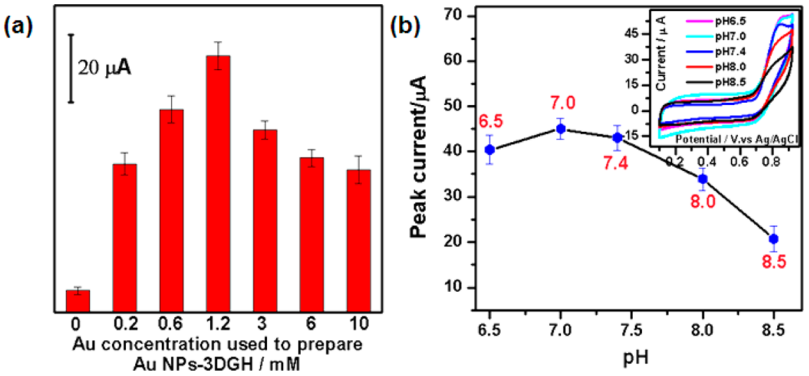

Figure 5. (a) Profile of the dependence of peak current on Au NPs−3DGH composite prepared with different Au concentrations. The Au concentrations ranged from 0 to 10 mM. (b) Plot of the dependence of the peak current on pH (from 6.5 to 8.5). Inset: CV curves of a Au NPs−3DGH modified electrode in 0.01 M PBS solution with different pH values containing 0.5 mM NO.

DOI: 10.1021/am5077777
ACS Appl. Mater. Interfaces 2015, 7, 2726−2734

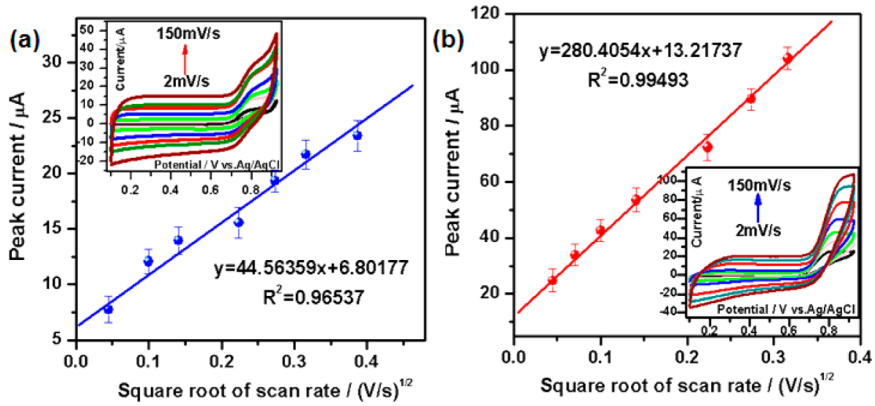

Figure 6. Plots of the dependence of the anodic peak current on the square root of scan rates: (a) Au NPs−2DG modified electrode and (b) Au NPs−3DGH modified electrode. Insets: CV curves of different scan rate studies of each electrode in 0.01 M PBS (pH 7.4). Scan rate in the range of 2−150 mV/s.

Scheme 1. Diagram of the Catalytic Mechanism of the Au NPs−3DGH Nanocomposite toward NO

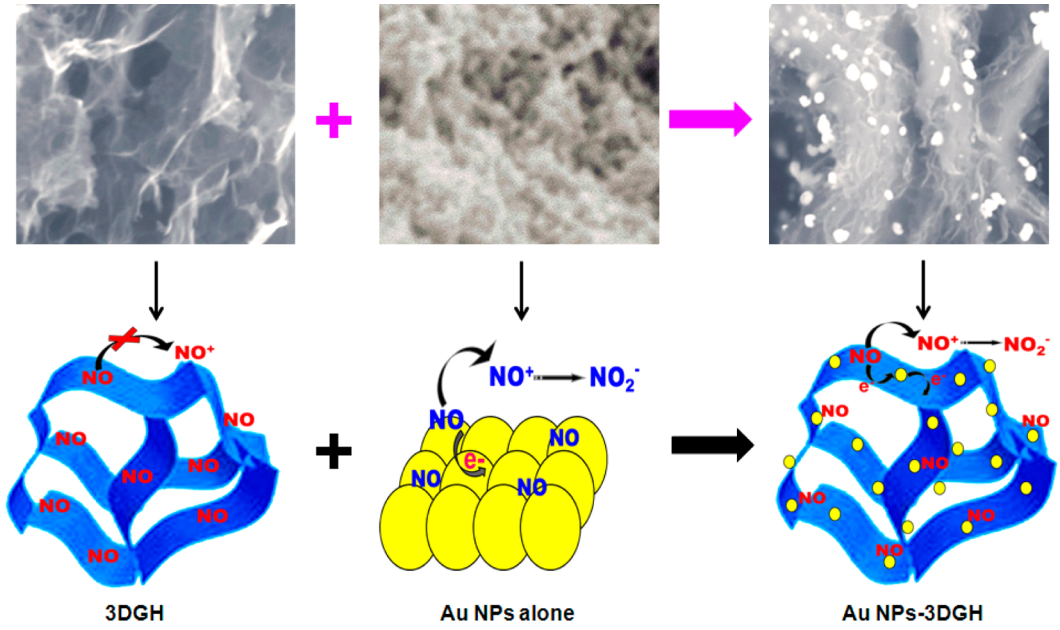

followed by converting NO^+ rapidly to NO_2^- via a chemical reaction:[24]

$$NO - e^- \rightarrow NO^+ \quad (1)$$

$$NO^+ + OH^- \rightarrow HNO_2 \rightarrow H^+ + NO_2^- \quad (2)$$

The CV for both Au NPs−2DG and Au NPs−3DGH modified electrodes clearly shows that the NO reactions are irreversible, while they possess a diffusion-control nature, and the relation of peak current vs $\upsilon^{1/2}$ is expressed as[45]

$$I_p = (2.99 \times 10^5)\alpha^{1/2} A C_0 D_0^{1/2} \upsilon^{1/2} \quad (3)$$

where α is the transfer coefficient, A is the electrochemical active surface area (EASA, cm^2), C_0 is the bulk concentration of NO (mol/L), D_0 is the diffusion coefficient of NO in solution ($cm^2\ s^{-1}$), and υ is the scan rate (V/s). The slope (k) of I_p vs $\upsilon^{1/2}$ ($2.99 \times 10^5)\alpha^{1/2} A C_0 D_0^{1/2}$) can be obtained by fitting eq 3. The fitted k values are 280.41 and 44.56 respectively. Since the α, C_0, and D_0 parameters in the k expression are constants for both the modified electrodes, the difference in k is apparently contributed by A, the electrochemical active surface area. Thus, the electrochemical active surface area of Au NPs−3DGH is much larger than that of Au NPs-2DG's by ∼6 times, resulting in the much higher peak current. The larger reaction surface area should be mainly attributed to the 3D graphene hydrogel allowing growth of a large amount of uniformly distributed Au NPs on its surface to electrocatalyze NO oxidation. The mechanism to enhance the NO oxidation on Au NPs−3DGH is schematically shown in Scheme 1, which illustrates that 3DGH has poor intrinsic electrocatalytic activity due to its carbon nature, but it offers huge active specific surface area, allowing Au NPs to load with a larger amount, smaller diameters, and more uniform distribution for effective electron transport and active sites toward NO oxidation. Thus, the unique Au NPs−3DGH nanocomposite structure can allow a large amount of NO molecules to absorb on the large amount of Au nanoparticle active centers, followed by fast electron loss to form NO^+ in terms of eq 1. Due to the highly porous Au NPs−3DGH nanocomposite structure, a high mass transport of NO^+ can be expected to meet OH^- to produce NO_2^-, as eq 2, for completion of the NO oxidation process. Apparently, the

DOI: 10.1021/am5077777
ACS Appl. Mater. Interfaces 2015, 7, 2726−2734

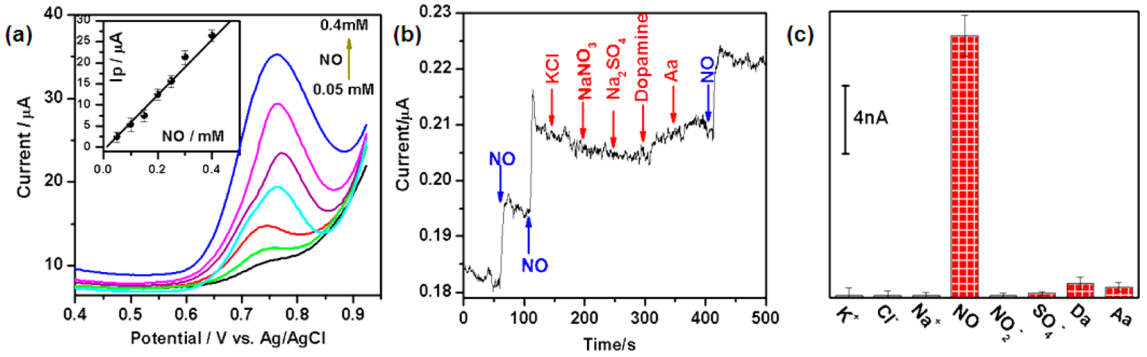

Figure 7. (a) Differential pulse voltammograms of the Au NPs−3DGH modified electrode at different NO concentrations. Inset: calibration plot of the dependence of the measured current on NO concentrations. Scan rate: 50 mV/s. (b) Amperometric curve for the study of the selectivity of Au NPs−3DGH composite modified electrode. (c) The selective profile.

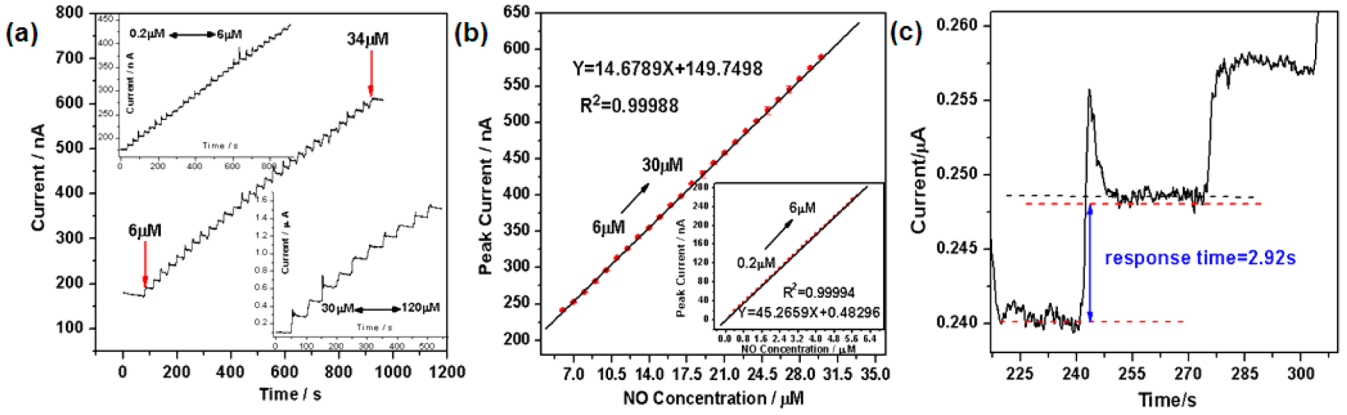

Figure 8. (a) Typical amperometric curve recorded at +0.81 V in PBS (pH 7.4) for Au NPs−3DGH composite modified electrode successively injected with 2 μL (0.2−6 μM), 10 μL (6−34 μM), and 100 μL (30−120 μM) of NO (1 nM) each time, respectively. (b) Linear calibration plot of the response current vs the nitric oxide concentration. (c) The response time.

synergy of Au NPs and 3DGH in the nanostructure bestows the excellent performance.

Differential pulse voltammetry (DPV), which can suppress the noise to improve the signal-to-noise ratio (S/N), was used to investigate the amperometric responses on the Au NPs−3DGH modified electrode toward NO oxidation (Figure 7a), and DPV showed a linear relation of peak current versus NO concentration (inset of Figure 7a) in a range of 0.05−0.4 mM. The selectivity of Au NPs−3DGH modified electrode for NO oxidation was studied with common interfering species in a biological system, such as NO_2^-, ascorbic acid, dopamine, and various ions (Figure 7c,d), showing that the Au NPs−3DGH modified electrode has a remarkably larger current response for NO oxidation (1 μM NO) than that resulting from these interfering species with the same concentration of 1 μM and thus offering excellent selectivity.

To characterize the sensing performance of the Au NPs−3DGH electrode toward NO oxidation, time-based amperometric measurement by successive additions of nitric oxide-containing solution at 0.81 V, as shown in Figure 8a, was performed, and it showed a significant increase of the oxidation current upon addition of NO solution. The response time determined from Figure 8c is 2.92 s. The relation of the oxidation peak current vs the concentration of nitric oxide is linear over a range from 0.2 to 6 μM with a detection limit of 9 nM NO (S/N = 3) (Figure 8b).

The Au NPs−3DGH modified electrode was used to in situ to detect NO released from both normal skin cell JB6-C30 and tumor cell B16-F10 by measuring the amperometric response at a constant potential of 0.81 V vs Ag/AgCl in the cell culture medium. To study the essential roles in the important biological process, acetylcholine (Ach) has been reported as a stimulus in living cells to generate NO by activating nitric oxide synthase (NOS), while hemoglobin (Hb) is one of the typical drugs to inhibit NO release.[46,47] The action of Au NPs−3DGH modified electrode toward different concentrations of Ach and Hb was investigated, as shown in Figure 9, in which the arrows indicate the injecting time of the drug. Figure 9b,e shows that there were no significant current changes (black) when 1 mM Ach was added in the culture medium but without culture cells. However, when 1 mM Ach and 1 mM Hb were simultaneously injected into a culture medium with a density of 1×10^4 cells [(b) JB6-C30 cells and (e) B16-F10 cells], the current only increases insignificantly, followed shortly by decreasing, indicating that Hb can effectively inhibit NO generation, even when adding the stimulus (light blue). In contrast, a sharply increased current upon Ach stimulation (blue and red) can be observed in JB6-C30 cells and B16-F10 cells medium, respectively, and the released NO is proportional to the concentration of the stimulus (Figure 9c,f). The nitric oxide releases from both JB6-C30 and B16-F10 living cells are also drug-concentration dependent, where the released NO concentration from JB6-C30 normal cells is 0.2705 and 0.4107 μM at 0.5 and 1 mM Ach stimulation, respectively, while for B16-F10 tumor cells, released NO is 1.3147 and 2.9255 μM at 0.5 and 1 mM Ach stimulation, respectively. Most

DOI: 10.1021/am5077777
ACS Appl. Mater. Interfaces 2015, 7, 2726−2734

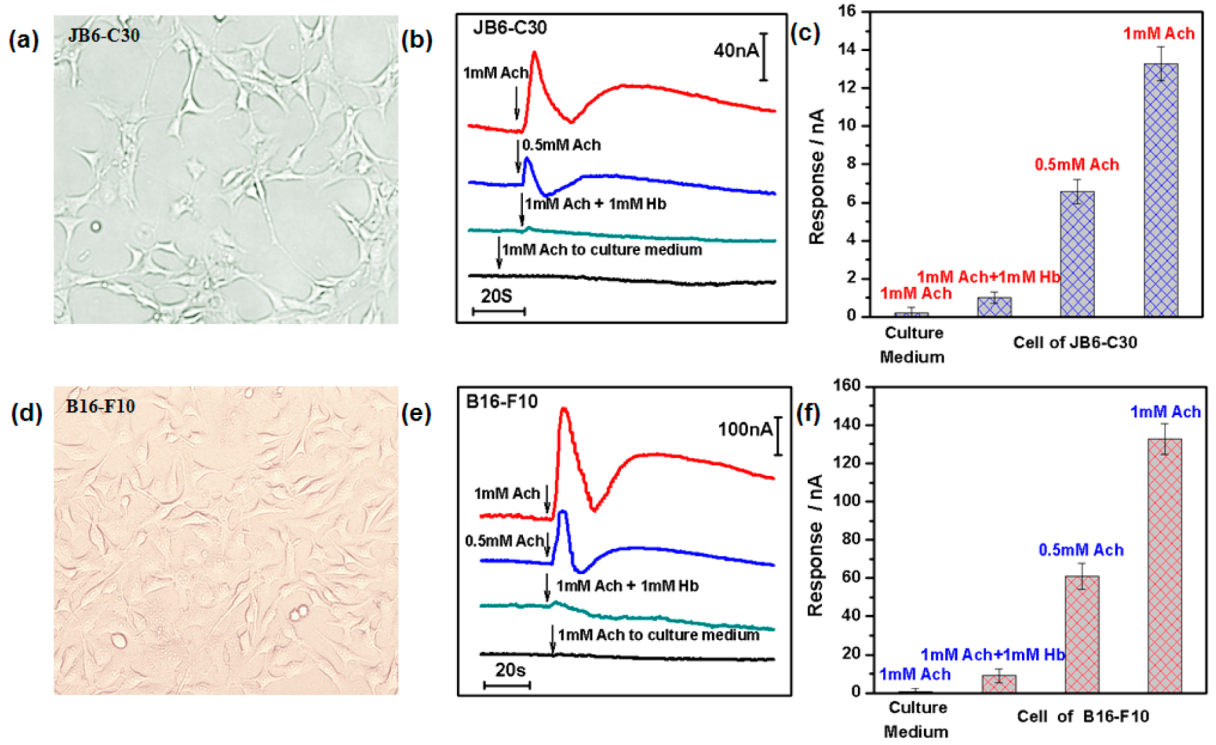

Figure 9. Microscope photos of normal mice skin cell JB6-C30 (a) and tumor cell B16-F10 (d) in a culture dish with a cell density of 1×10^4. In situ detection of nitric oxide molecule released from the JB6-C30 cells (b) and B16-F10 cells (e) in cell culture medium, and the drugs were added at the time indicated by the arrows. Parts c and f are profiles corresponding to parts b and e, respectively.

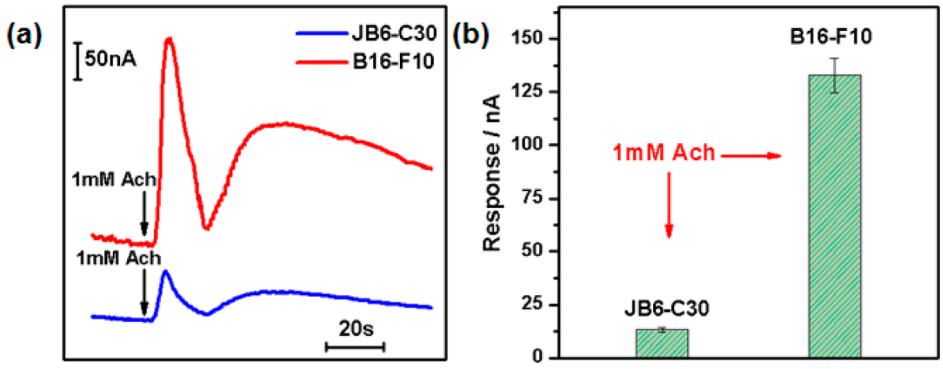

Figure 10. (a) In situ detection under 1 mM Ach stimulation of nitric oxide molecule released from the normal cells JB6-C30 (blue) and tumor cells B16-F10 (red) in cell culture medium with a cell density of 1×10^4. The drugs were added at the time indicated by the arrows. (b) Profiles corresponding to part a.

importantly, the concentration of released NO from the skin tumor cell is remarkably higher than that of the normal skin cell by 1 order of magnitude. It is noted that a first sharp, capacitive-like peak occurs followed by second prominent wave for both JB6-C30 and B16-F10 cells after addition of the stimulus. A similar result has been reported in the in situ detection of glutamate[48,49] and NO[50] released from brain cells. It is suggested to be attributed to some electroactive side products (such as serotonin and dopamine) being coreleased from the cell after the stimulation rather than NO. Despite the good selectivity, the side products released temporarily and suddenly with very high concentration; however, they do not interfere with the NO oxidation signal. Thus, it is reasonable to use this explanation for the results we observed as in Figure 9b,e.

Nitric oxide released from normal and tumor cells under the drug stimulations with the same concentration was in situ detected to investigate the essential role of NO in the disease pathology process (Figure 10). When 1 mM Ach was added to the culture medium with a density of 1×10^4 normal cell JB6-C30 and tumor cell B16-F10, respectively, the response currents changed differently (Figure 10a). The tumor cell B16-F10 (red) has a response ~5 times as large as that of normal cell JB6-C30 (blue) (Figure 10b). Such a large difference in response of NO release between the normal and tumor cells is because the NOS in tumor cells has a much higher expression than in normal ones,[51] so then more NOS molecules can be activated by Ach to generate more nitric oxide molecules. It is understandable that the higher expression of NOS in tumor cells is due to the vital role of nitric oxide in promoting the tumor progression and metastasis directly by inducing the proliferation, migration, and invasion and indirectly by expressing angiogenic and lymphangiogenic

DOI: 10.1021/am5077777
ACS Appl. Mater. Interfaces 2015, 7, 2726−2734

factors.[51,52] Therefore, when the same concentration of Ach was injected, the NO release in tumor cells was much higher than in the normal ones. The results indicate that the NO released from cells could be directly related with the progress of melanoma formation, thus holding great promise for us to understand the critical pathological process of melanoma through in situ detection of NO, while a simple approach for clinic diagnosis and prognosis of tumors is rendered.

4. CONCLUSIONS

We successfully developed a facile approach to grow Au nanoparticles on highly porous 3D graphene hydrogel with large electroactive surface area and high electrocatalytic activity toward NO oxidation, showing a low detection limit, fast response time, and excellent selectivity for NO sensing. The Au NPs−3DGH also demonstrates excellent ability to in situ detect nitric oxide released from living cells, revealing that the tumor cell B16-F10 releases 5 times more NO than the normal cell JB6-C30. The in situ detected nitric oxide from living cells offers critical information for us to understand the melanoma, while can be used as an indicator for diagnosis and prognosis of skin cancers.

AUTHOR INFORMATION

Corresponding Author

*E-mail: ecmli@swu.edu.cn.

Notes

The authors declare no competing financial interest.

ACKNOWLEDGMENTS

This work is financially supported by National Science Foundation of China (No. 21205097), National Key Basic Research Program of China (973 Program) under contract No. 2013CB127804, Institute for Clean Energy & Advanced Materials (Southwest University, Chongqing, China), Chongqing Key Laboratory for Advanced Materials and Technologies of Clean Energies (Chongqing, China), start-up grant under SWU111071 from Southwest University (Chongqing, China), Chongqing Engineering Research Center for Rapid Diagnosis of Dread Disease (Chongqing, China), and Chongqing development and reform commission, Southwest University (Chongqing, China).

REFERENCES

(1) O'dell, T. J.; Hawkins, R. D.; Kandel, E. R.; Arancio, O. Tests of the Roles of Two Diffusible Substances in Long-Term Potentiation: Evidence for Nitric Oxide as a Possible Early Retrograde Messenger. *Proc. Natl. Acad. Sci. U. S. A.* **1991**, *88*, 11285−11289.

(2) Bredt, D. S.; Snyder, S. H. Nitric Oxide Mediates Glutamate-Linked Enhancement of cGMP Levels in the Cerebellum. *Proc. Natl. Acad. Sci. U. S. A.* **1989**, *86*, 9030−9033.

(3) Garthwaite, J.; Garthwaite, G.; Palmer, R. M.; Moncada, S. NMDA Receptor Activation Induces Nitric Oxide Synthesis from Arginine in Rat Brain Slices. *Mol. Pharmacol.* **1989**, *172*, 413−416.

(4) Schuman, E. M.; Madison, D. V. A Requirement for the Intercellular Messenger Nitric Oxide in Long-Term Potentiation. *Science* **1991**, *254*, 1503−1506.

(5) Marletta, M. A.; Yoon, P. S.; Iyengar, R.; Leaf, C. D.; Wishnok, J. S. Macrophage Oxidation of L-Arginine to Nitrite and Nitrate: Nitric Oxide Is an Intermediate. *Biochemistry* **1988**, *27*, 8706−8711.

(6) Furchgott, R. F.; Vanhoutte, P. M. Endothelium-Derived Relaxing and Contracting Factors. *FASEB J.* **1989**, *3*, 2007−2018.

(7) Lala, P. K.; Chakraborty, C. Role of Nitric Oxide in Carcinogenesis and Tumour Progression. *Lancet Oncol.* **2001**, *2*, 149−156.

(8) Lala, P. Significance of Nitric Oxide in Carcinogenesis, Tumor Progression and Cancer Therapy. *Cancer Metastasis Rev.* **1998**, *17*, 1−6.

(9) Li, C. M.; Zang, J.; Zhan, D.; Chen, W.; Sun, C. Q.; Teo, A. L.; Chua, Y.; Lee, V.; Moochhala, S. Electrochemical Detection of Nitric Oxide on a SWCNT/RTIL Composite Gel Microelectrode. *Electroanalysis* **2006**, *18*, 713−718.

(10) Peach, M. J.; Singer, H. A.; Izzo, N. J.; Loeb, A. L. Role of Calcium in Endothelium-Dependent Relaxation of Arterial Smooth Muscle. *Am. J. Cardiol.* **1987**, *59*, A35−A43.

(11) Archer, S. L.; Rist, K.; Nelson, D. P.; DeMaster, E. G.; Cowan, N.; Weir, E. K. Comparison of the Hemodynamic Effects of Nitric Oxide and Endothelium-Dependent Vasodilators in Intact Lungs. *J. Appl. Physiol.* **1990**, *68*, 735−747.

(12) Kontos, H. A.; Wei, E. P.; Kukreja, R. C.; Ellis, E. F.; Hess, M. L. Differences in Endothelium-Dependent Cerebral Dilation by Bradykinin and Acetylcholine. *Am. J. Physiol.* **1990**, *258*, H1261−H1266.

(13) Bryan, N. S.; Grisham, M. B. Methods To Detect Nitric Oxide and Its Metabolites in Biological Samples. *Free Radical Biol. Med.* **2007**, *43*, 645−657.

(14) Archer, S. Measurement of Nitric Oxide in Biological Models. *FASEB J.* **1993**, *7*, 349−360.

(15) Ciszewski, A.; Milczarek, G. A New Nafion-Free Bipolymeric Sensor for Selective and Sensitive Detection of Nitric Oxide. *Electroanalysis* **1998**, *10*, 791−793.

(16) Kikuchi, K.; Nagano, T.; Hayakawa, H.; Hirata, Y.; Hirobe, M. Real Time Measurement of Nitric Oxide Produced Ex Vivo by Luminol−H_2O_2 Chemiluminescence Method. *J. Biol. Chem.* **1993**, *268*, 23106−23110.

(17) Haklar, G.; Sayin-Özveri, E.; Yüksel, M.; Aktan, A. Ö.; Yalçin, A. S. Different Kinds of Reactive Oxygen and Nitrogen Species Were Detected in Colon and Breast Tumors. *Cancer Lett.* **2001**, *165*, 219−224.

(18) Qi, K.; Qiu, H.; Rutherford, J.; Zhao, Y.; Nance, D. M.; Orr, F. W. Direct Visualization of Nitric Oxide Release by Liver Cells after the Arrest of Metastatic Tumor Cells in the Hepatic Microvasculature. *J. Surg. Res.* **2004**, *119*, 29−35.

(19) Nakatsubo, N.; Kojima, H.; Sakurai, K.; Kikuchi, K.; Nagoshi, H.; Hirata, Y.; Akaike, T.; Maeda, H.; Urano, Y.; Higuchi, T. Improved Nitric Oxide Detection Using 2,3-Diaminonaphthalene and Its Application to the Evaluation of Novel Nitric Oxide Synthase Inhibitors. *Biol. Pharm. Bull.* **1998**, *21*, 1247−1250.

(20) Loibl, S.; von Minckwitz, G.; Weber, S.; Sinn, H. P.; Schini-Kerth, V. B.; Lobysheva, I.; Nepveu, F.; Wolf, G.; Strebhardt, K.; Kaufmann, M. Expression of Endothelial and Inducible Nitric Oxide Synthase in Benign and Malignant Lesions of the Breast and Measurement of Nitric Oxide Using Electron Paramagnetic Resonance Spectroscopy. *Cancer* **2002**, *95*, 1191−1198.

(21) Lecour, S.; Chevet, D.; Maupoil, V.; Moisant, M.; Bernard, C.; Zahnd, J. P.; Touchard, G.; Briot, F.; Rochette, L. Intrarenal Detection of Nitric Oxide Using Electron Spin Resonance Spectroscopy in Hypertensive Lipopolysaccharide-Treated Rats. *J. Cardiovasc. Pharmacol.* **2002**, *40*, 9−17.

(22) Kim, I. K.; Chung, H. T.; Oh, G. S.; Bae, H. O.; Kim, S. H.; Chun, H. J. Integrated Gold-Disk Microelectrode Modified with Iron(II)-Phthalocyanine for Nitric Oxide Detection in Macrophages. *Microchem. J.* **2005**, *80*, 219−226.

(23) Wadsworth, R.; Stankevicius, E.; Simonsen, U. Physiologically Relevant Measurements of Nitric Oxide in Cardiovascular Research Using Electrochemical Microsensors. *J. Vasc. Res.* **2005**, *43*, 70−85.

(24) Tarpey, M. M.; Fridovich, I. Methods of Detection of Vascular Reactive Species Nitric Oxide, Superoxide, Hydrogen Peroxide, and Peroxynitrite. *Circ. Res.* **2001**, *89*, 224−236.

(25) Gomes, A.; Fernandes, E.; Lima, J. L. Use of Fluorescence Probes for Detection of Reactive Nitrogen Species: A Review. *J. Fluoresc.* **2006**, *16*, 119−139.

DOI: 10.1021/am5077777
ACS Appl. Mater. Interfaces 2015, 7, 2726−2734

(26) Villamena, F. A.; Zweier, J. L. Detection of Reactive Oxygen and Nitrogen Species by EPR Spin Trapping. *Antioxid. Redox Signaling* **2004**, *6*, 619−629.
(27) Kasai, S.; Shiku, H.; Torisawa, Y.-s.; Noda, H.; Yoshitake, J.; Shiraishi, T.; Yasukawa, T.; Watanabe, T.; Matsue, T.; Yoshimura, T. Real-Time Monitoring of Reactive Oxygen Species Production during Differentiation of Human Monocytic Cell Lines (THP-1). *Anal. Chim. Acta* **2005**, *549*, 14−19.
(28) Kojima, H.; Nakatsubo, N.; Kikuchi, K.; Kawahara, S.; Kirino, Y.; Nagoshi, H.; Hirata, Y.; Nagano, T. Detection and Imaging of Nitric Oxide with Novel Fluorescent Indicators: Diaminofluoresceins. *Anal. Chem.* **1998**, *70*, 2446−2453.
(29) Rodriguez-Rodriguez, R.; Simonsen, U. Measurement of Nitric Oxide and Reactive Oxygen Species in the Vascular Wall. *Curr. Anal. Chem.* **2012**, *8*, 485−494.
(30) Cai, H.; Dikalov, S.; Griendling, K. K.; Harrison, D. G. Detection of Reactive Oxygen Species and Nitric Oxide in Vascular Cells and Tissues. *In Vascular Biology Protocols*; Springer: New York, 2007; pp 293−311.
(31) Taha, Z. H. Nitric Oxide Measurements in Biological Samples. *Talanta* **2003**, *61*, 3−10.
(32) Bedioui, F.; Quinton, D.; Griveau, S.; Nyokong, T. Designing Molecular Materials and Strategies for the Electrochemical Detection of Nitric Oxide, Superoxide and Peroxynitrite in Biological Systems. *Phys. Chem. Chem. Phys.* **2010**, *12*, 9976−9988.
(33) Griveau, S.; Seguin, J.; Scherman, D.; Chabot, G. G.; Bedioui, F. In Vivo Electrochemical Detection of Nitroglycerin-Derived Nitric Oxide in Tumor-Bearing Mice. *Electroanalysis* **2009**, *21*, 631−634.
(34) Katrlík, J.; Zálešáková, P. n. Nitric Oxide Determination by Amperometric Carbon Fiber Microelectrode. *Bioelectrochemistry* **2002**, *56*, 73−76.
(35) Wang, Y.; Li, Q.; Hu, S. A Multiwall Carbon Nanotubes Film-Modified Carbon Fiber Ultramicroelectrode for the Determination of Nitric Oxide Radical in Liver Mitochondria. *Bioelectrochemistry* **2005**, *65*, 135−142.
(36) Pereira-Rodrigues, N.; Albin, V.; Koudelka-Hep, M.; Auger, V.; Pailleret, A.; Bedioui, F. Nickel Tetrasulfonated Phthalocyanine Based Platinum Microelectrode Array for Nitric Oxide Oxidation. *Electrochem. Commun.* **2002**, *4*, 922−927.
(37) Gu, H.-Y.; Yu, A.-M.; Yuan, S.-S.; Chen, H.-Y. Amperometric Nitric Oxide Biosensor Based on the Immobilization of Hemoglobin on a Nanometer-Sized Gold Colloid Modified Au Electrode. *Anal. Lett.* **2002**, *35*, 647−661.
(38) Shibuki, K. An Electrochemical Microprobe for Detecting Nitric Oxide Release in Brain Tissue. *Neurosci. Res.* **1990**, *9*, 69−76.
(39) Griveau, S.; Bedioui, F. Overview of Significant Examples of Eectrochemical Sensor Arrays Designed for Detection of Nitric Oxide and Relevant Species in a Biological Environment. *Anal. Bioanal. Chem.* **2013**, *405*, 3475−3488.
(40) He, Q.; Zheng, D.; Hu, S. Development and Application of a Nano-Alumina Based Nitric Oxide Sensor. *Mikrochim. Acta* **2009**, *164*, 459−464.
(41) Merkoçi, A. Nanobiomaterials in Electroanalysis. *Electroanalysis* **2007**, *19*, 739−741.
(42) Ratinac, K. R.; Yang, W.; Gooding, J. J.; Thordarson, P.; Braet, F. Graphene and Related Materials in Electrochemical Sensing. *Electroanalysis* **2011**, *23*, 803−826.
(43) Xu, Y.; Sheng, K.; Li, C.; Shi, G. Self-Assembled Graphene Hydrogel via a One-Step Hydrothermal Process. *ACS Nano* **2010**, *4*, 4324−4330.
(44) Cong, H.-P.; Ren, X.-C.; Wang, P.; Yu, S.-H. Macroscopic Multifunctional Graphene-Based Hydrogels and Aerogels by a Metal Ion Induced Self-Assembly Process. *ACS Nano* **2012**, *6*, 2693−2703.
(45) Bard, A. J.; Faulkner, L. R. *Electrochemical Methods: Fundamentals and Applications*; Wiley: New York, 1980; Vol. 2.
(46) Cohen, R. A.; Vanhoutte, P. M. Endothelium-Dependent Hyperpolarization Beyond Nitric Oxide and Cyclic GMP. *Circulation* **1995**, *92*, 3337−3349.
(47) Schechter, A. N.; Gladwin, M. T. Hemoglobin and the Paracrine and Endocrine Functions of Nitric Oxide. *N. Engl. J. Med.* **2003**, *348*, 1483−1485.
(48) Burmeister, J. J.; Pomerleau, F.; Palmer, M.; Day, B. K.; Huettl, P.; Gerhardt, G. A. Improved Ceramic-Based Multisite Eicroelectrode for Rapid Measurements of L-Glutamate in the CNS. *J. Neurosci. Methods* **2002**, *119*, 163−171.
(49) Walker, E.; Wang, J.; Hamdi, N.; Monbouquette, H. G.; Maidment, N. T. Selective Detection of Extracellular Glutamate in Brain Tissue Using Microelectrode Arrays Coated with Over-Oxidized Poly Pyrrole. *Analyst* **2007**, *132*, 1107−1111.
(50) Barbosa, R. M.; Lourenço, C. F.; Santos, R. M.; Pomerleau, F.; Huettl, P.; Gerhardt, G. A.; Laranjinha, J. In Vivo Real-Time Measurement of Nitric Oxide in Anesthetized Rat Brain. *Methods Enzymol.* **2008**, *441*, 351−367.
(51) Lala, P. K.; Chakraborty, C. Role of Nitric Oxide in Carcinogenesis and Tumour Progression. *Lancet Oncol.* **2001**, *2*, 149−156.
(52) Fukumura, D.; Kashiwagi, S.; Jain, R. K. The Role of Nitric Oxide in Tumour Progression. *Nat. Rev. Cancer* **2006**, *6*, 521−534.

DOI: 10.1021/am5077777
ACS Appl. Mater. Interfaces 2015, 7, 2726−2734